Design and Diagnosis of high-performance CO_2-to-CO electrolyzer cells

Sven Brückner [a], Quanchen Feng[a], Wen Ju*[a], Daniela Galliani[b], Anna Testolin[b], Malte Klingenhof[a], Sebastian Ott[a], Peter Strasser*[a]

*Corresponding author: Wen Ju, ju@tu-berlin.de; Peter Strasser, pstrasser@tu-berlin.de

Affiliation

[a] *Department of Chemistry, Chemical Engineering Division, Technical University Berlin, Berlin 10623, Germany*

[b] *Industrie De Nora, Research and Development Department, via Leonardo Bistolfi 35, 20134, Milan, Italy*

Abstract

This work reports the design of a highly efficient neutral-pH CO_2-to-CO zero-gap electrolyzer incorporating a new family of 2D layered framework-derived mesoporous single atom NiNC catalysts. What sets its performance apart from previous reports is not only the ~100% CO faradaic efficiency at applied current densities of up to 300 mA cm^{-2} at just above 3 V cell voltage and 40% total energy efficiency, but the uniquely low stoichiometric CO_2 excess, λ_{stoich}, of 1.2 that yields a molar CO concentration of around 70%$_{Vol}$ in the electrolyzer exit stream at 40% single pass CO_2 conversion. This CO-rich exit stream and the low cost catalyst makes this electrolyze design ideally suited for cost-effective and energy efficient tandem cell configurations for high C_{2+} product yields. We also propose and validate a new kinetic diagnostic tool to help resolve mechanisms of undesired CO_2 loss. We introduce an experimentally accessible carbon crossover coefficient, CCC, that describes the ratio between non-catalytic acid-base CO_2 consumption and catalytically generated alkalinity. It offers an intuitive insight into the nature of the prevalent ionic transport. Combined with the λ_{stoich} and the faradaic CO efficiency data, the CCC analysis offers practical guidelines toward improved electrolyzer designs. Our CCC-based cell diagnosis can be applied more broadly to all CO_2 electrolyzers

Introduction

CO_2 emissions increase drastically due to the fast-growing global fossil-based energy demand, leading to urgent environmental crises such as climate change and ocean acidification. To mitigate CO_2 emissions, technologies related to the capture and reuse of CO_2 from the atmosphere or point sources are moving to the fore.

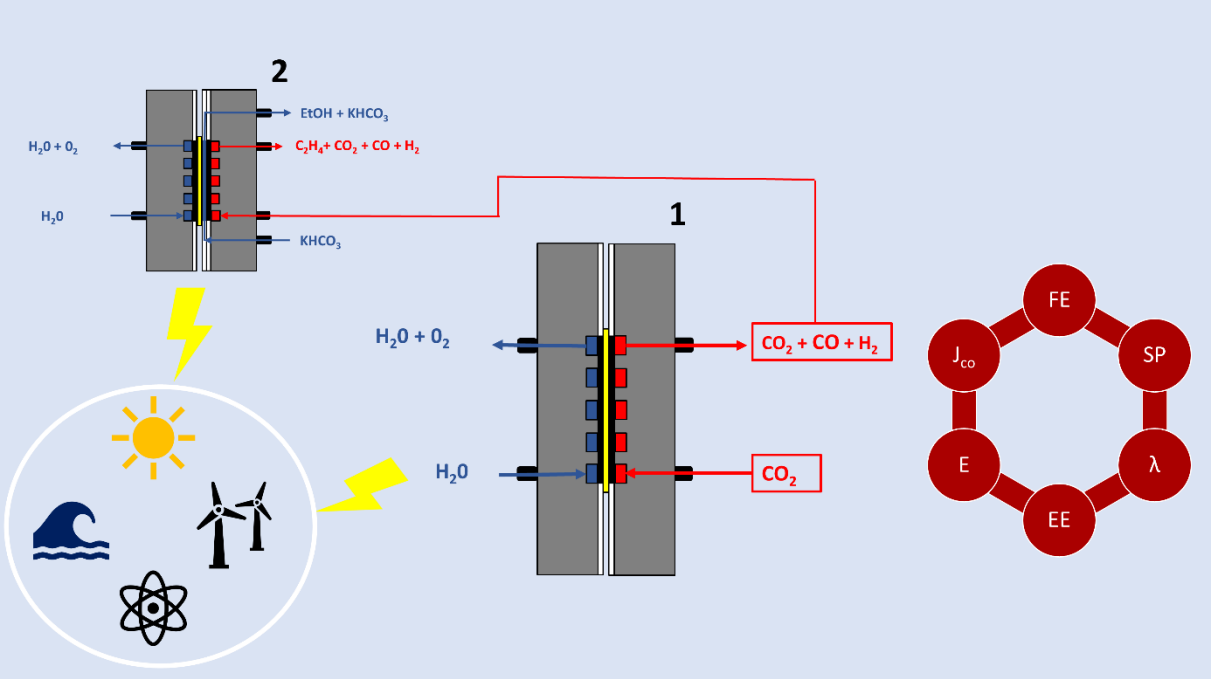

Figure 1: **The Tandem Electrolyzer concept coupling a CO_2 to CO electrolyzer ("cell 1") directly to a CO to C_{2+} electrolyzer ("cell 2") to close the CO_2 cycle using value-added C1-C3 products.** Efficient CO_2 use is enabled by a Tandem Electrolysis Cell concept powered by renewables to produce chemicals and fuels. The Tandem Cell concept offers maximal materials and operational flexibility for Cell 1 and Cell 2. In cell 1, the captured CO_2 will be converted to high purity CO-rich feeds that enter cell 2 for the electrochemical C-C coupling. State of art design suffer from low molar CO concentrations in the exit feed. Relevant performance indicators emphasized in the red hexagonal scheme are the partial CO current densities (J_{CO}), Faradaic CO efficiency (FE), Cell potential (E), energy efficiency (EE), stoichiometric excess of CO2 (λ) and single pass CO_2-to-CO conversion (SP) (**Supplementary Table 1**).

Direct electrochemical CO_2 reduction reaction (CO2RR) is a process route to convert CO_2 into valorized products via multiple electron-transfer reaction steps, with renewable electricity as the driving force.[1-11] Catalyzing multi-electron reaction cascades at one and the same electrode, catalyst, or even molecular active site results in compromised, usually suboptimal overall reactivities. Owing to their design flexibility, however, tandem electrode and tandem cell

designs raise overall efficiencies and product yields of multi-electron processes by enabling optimized operation points for individual process steps.[12] To technologically implement a coupled tandem cell design for the CO2RR, CO-rich streams supplied by a "CO_2-to-CO" electrolyzer (Cell 1 in **Figure 1**) will be fed into the "CO-to-X" electrolyzer (Cell 2 in Figure 1) for downstream production of C_{2+} chemicals and fuels (**Figure 1**).[13] To make this tandem cell scheme viable, a faradaic 100% efficient CO_2-to-CO electrolysis cell 1 operating at industrially relevant current densities, at high CO space time yield, Y^{SP}_{CO}, at high catalytic CO_2 utilization, $\eta^{cat}_{CO_2}$, at high total energy efficiencies, EE, and high pass conversion, SP, must be designed at very low, near unity stoichiometric CO_2 excess, λ. While catalyst screenings and idealized cell conditions can optimize each of these perfomrnace parameters (Supplementary Table 1) individually, the simultaenous optimization and analysis of all this performance parameters in operating CO_2-to-CO electrolyzers has remained elusive. Despite near 100% faradaic efficiency for CO, the exit flow compositions of previously reported CO_2-to-CO electrolyzers have typically remained very CO_2 rich, as the cells were not operated at low enough (<2) stoichiometric ratios, λ, nor high enough single pass conversions, SP, nor high enough catalytic CO_2 utilizations, $\eta^{cat}_{CO_2}$. As a result, previously published CO_2-to-CO electrolyzer cell designs failed to offer tandem design advantages over pure CO_2 feeds to Cell 2. This is why new cathode catalysts and cathode layer designs, as well as a cell-level diagnostic analysis and control of cell parameters such as the stoichiometric ratio, λ, single pass conversion, SP, or the CO_2 utilization, $\eta^{cat}{}_{CO_2}$, of cell 1 are required to fully unfold kinetic benefits of the combined coupled cascade. While much past work was dedicated to understand, and design the atomic-scale catalytic active sites of individual CO2RR catalyst materials, future work need to place equal focus on a thorough diagnosis and design of the dynamic operation points of the triple phase cathode layers of CO_2-to-CO electrolyzers. This work contributes to that.

As far as viable electrocatalysts for the CO_2-to-CO electrolyzer (cell 1) are concerned, oxide-derived metallic Ag continues to be the state-of-art cathode catalyst under operando condition with good CO efficiency.[14-16] In Ag-derived gas diffusion electrode (GDE) flow electrolyzers, CO activity has been repeatedly reported up to 600 mA cm^{-2} current densities, yet combined with low efficiencies.[17-23] Given its critical materials nature, large-scale utilization of Ag at today's metal loadings faces stiff resource and cost challenges. More seriously, Ag suffers from cathodic corrosion at CO2RR electrode potentials, resulting in unstable catalyst films. Starting

from the initial report in 2015,[24] a new class of nickel-nitrogen-doped carbon (Ni-N-C) single metal site catalyst was developed to meet these challenges.[24-30] In H-type liquid electrolyte reactors, these PGM-free catalysts deliver comparable CO reactivity as Ag-based ones, yet require only minute (< 1 wt%) metal doping vs thick sputtered or particle layers of Ag black metal loadings, offering a vast materials cost advantage. In addition, unlike bulk metal films, the Ni-N-C catalysts possess tunable pore structures ranging from micro to meso porosity combined with large surface areas, which benefit mass transport and raise mass-based catalytic activities. Despite these features, key performance metrics of Ni-N-C catalyst layers in membrane/gas diffusion electrode assemblies incorporated in flow electrolyzer have remained poor compared to commercial, state-of-art Ag electrodes. In addition, most electrolyzer reports to date operated the CO electrolyzers at differential flow conditions of large CO_2 excess compared to CO_2 consumption, equivalent to very large stoichiometric ratios λ_{stoich} (= $CO_{2,\,in}$ / $CO_{2,\,consumed}$), often using high alkaline electrolyte. This resulted in poor single pass conversions and favored carbon loss across the membrane. Viable "CO_2-to-CO" electrolyzer cathodes need to not only show 100% faradaic CO efficiency and high partial current density, but they have to show this at very low λ values to push the molar CO content in the exit feed toward unity. High molar CO ratios in the exit feed benefit the catalytic conversion rates and product efficiencies in the downstream electrocatalytic CO-to-C_{2+} reactions in cell 2 of **Figure 1**. This work will address this unmet need highlighting an efficient precious metal-free "CO_2-to-CO" electrolyzer cathode design, along with a novel diagnostic approach of its catalytic and mass transport characteristics.

This work reports a new cathode catalyst and cell design of a high performance AEM CO_2-to-CO flow electrolyzer operated with a noble-metal free gas diffusion cathode at neutral pH displaying a previously unachieved set of favorable performance indicators. What sets the present electrolyzer apart from previous designs is the use of a new imidazole-derived Ni-N-C single metal atom cathode catalyst deployed in a zero-gap gas diffusion electrode layer with favorable kinetic and mass transport characteristics thanks to accessible pores and active sites. The design features essentially over 90% faradaic efficiencies at up to 250 mA cm^{-2} partial CO current density at high single pass conversion, high CO_2 utilization, and high energy efficiency, realized at to-date unachieved stoichiometric CO_2 excess ratios as low as ~ 1.2. Equally, important, this work introduces the *carbon crossover coefficient*, CCC, as a novel diagnostic tool and design parameter for electrocatalytic CO_2 reduction gas diffusion cathode layers. The CCC is experimentally accessible and provides insight in the mass transport characteristics of

CO_2 gas diffusion cathodes under varying flow and pH conditions. We evaluate the CCC and λ_{stoich} values as function of cell current and cathode layer thickness for two distinctly different Ni single atom cathode catalysts (imidazole-derived Ni-N-C and polyaniline-derived Ni-N-C). From this analysis, we diagnose the effectiveness of in-plane and through-plane ionic transport and validate our conclusions by microscopic analysis.

Results

Electrocatalyst synthesis, characterization and GDE manufacturing

A powder electrocatalyst characterized by nitrogen-coordinated single Ni atoms embedded in graphene layers (referred to henceforth as "NiNC" catalyst) was synthesized by pyrolysis of a Ni-imidazolate precursors (**Figure 2a**). This catalyst will henceforth be referred to as "NiNC-IMI". A benchmark polyanilin-derived NiNC electrocatalyst, referred to as NiNC-PANI served as reference catalyst. To characterizes the chemical state, composition, morphology, porosity, and microstructure of the two catalysts, a number of analytical techniques (**Supplementary Figure 1** to **3**), involving powder X-ray diffraction (XRD), transmission electron microscopy (TEM), and N_2 physisorption analysis were performed.

The XRD patterns (**Supplementary Figure 1)** reveal crystalline phases in the NiNC catalysts. Both NiNC-IMI and NiNC-PANI samples exhibit a pronounced diffraction peak at around 26°, assigned to the family of graphitic carbon planes. Additional Bragg peaks suggested the presence of a metallic Ni^0 phase, associated with (carbon-encapsulated) Ni nanoparticles in the bulk of the catalyst. It is well-documented that such Ni particles are chemically inert for the CO_2 reduction electrocatalysis.[28,30-33] The chemical state and elemental composition of the catalysts surface were obtained from the core level regions of C1s, N1s, and Ni2p(3/2) (**Figure 2b-e**). Carbon speciation is dominated by sp^2 hybridized moieties, showing a high carbonization degree. Following earlier analyses of MNC electrocatalysts, the N speciation was split into a few distinct fractions (**Supplementary Note 1**, **Supplementary Table 2**). The Ni2p3/2 core level region (**Figure 2e**) revealed the Ni chemical state near the surface up to a depth of about ~2-5nm. Three different Ni chemical states (metallic Ni in embedded particles and Ni^{1+}, Ni^{2+} in NiN_x site motifs) were identified (**Supplementary Table 3**).[34-37] In both NiNC-IMI and NiNC-PANI, Ni prevails in the chemical states of Ni^{2+} and Ni^{+}. These two chemical Ni states are commonly found for the N-coordinated, catalytically active single Ni atom sites.[31,38] The

overall elemental composition of either catalyst is very similar, with metallic Ni particles adding extra Ni at% for NiNC-IMI (**Supplementary Table 4**). The TEM micrographs in **Supplementary Figure 3** revealed the catalyst microstructures. Notably, NiNC-IMI exhibits a fiber-like backbone structure with homogeneously distributed diameters (~ 20 nm). In addition, carbon layer-embedded metallic Ni particles and pores (due to particle leaching) with constant size (5~10 nm) could be observed (**Supplementary Figure 3a-c**). By contrast, the NiNC-PANI shows a densely compacted layer-like backbone structure, and the encapsulated Ni particles vary from 10 to 50 nm diameters (**Supplementary Figure 3d-f**). However, no visible pores could be identified. These results are corroborated by the BET analysis. The NiNC-IMI showed a specific surface area of 220 m^2 g^{-1} with a large fraction of mesopores (~ 4-5 nm pore size). By contrast, NiNC-PANI provides a much higher surface area of 414 m^2 g^{-1}, due to the dominant microporosity (**Supplementary Figure 2**). These distinct powder characteristics will, as shown below, translate into characteristic differences in their cathode layers and, consequently, in the respective electrolyzer cell performances, reflected in their carbon crossover diagnosis introduced below. By combining the BET-surface area and the XPS near-surface fraction of $Ni^{1+/2+}$ species related to Ni-N_x motifs, we estimated[31] and compared the Ni-N_x surface site density (SD) to other NiNC catalysts (**Supplementary Note 2**, **Supplementary Figure 4**). NiNC-PANI and NiNC-IMI catalysts showed the highest exposed SD of all considered benchmark catalysts.

To explore the near-surface *site density*-normalized, intrinsic catalytic CO_2 reduction kinetics of the single Ni atom catalysts and contrast their respective *site accessibility*, partial CO current densities and CO turn over frequencies were derived for different catalyst loadings. This was carried out in a conventional liquid-electrolyte H-type cell and compared to a number of benchmark NiNC-catalysts (**Supplementary Figure 5-8**). Our two NiNC electrocatalysts in focus showed a peak 85-90% CO faradaic efficiency (FE_{CO}) at approximately -0.75 V_{RHE} (**Supplementary Figure 5a**). The NiNC-IMI displayed the highest CO mass activity (exceeding 25 mA mg^{-1}), thanks to its high active site density related to its mesoporous structure (**Supplementary Figure 5b**), closely followed by NiNC-PANI. Normalization of the mass (or equally geometric area) activity data using the Ni-Nx surface site density, almost identical intrinsic TOF vs E relations ensued.[31] This suggests the presence of similar active Ni-Nx motifs in the various NiNC catalysts (**Supplementary Figure 9**), which is surprising given the vastly different chemical nature of the synthetic pathways. Yet, it underscores the insensitivity of the emerging active site during pyrolysis to the chemical nature of the precursors. **Supplementary**

Figure 9 also reveals vastly different TOF-E trajectories for E < -0.75 V. This difference is not due to varying site densities, but due to varying site accessibility. Mesoporous catalysts (NiNC-IMI) offer enhanced site accessibility and suffer from local CO_2 depletion resulting in plateauing TOF-E relations. For a more in-depth analysis of the NiNC catalysts, different geometric loadings were tested (**Figure 2f-g**, **Supplementary Figure 6-7**) and the results showed that both catalysts are influenced by the loading but it seems that the lower loadings of NiNC-IMI outperform the NiNC-PANI especially in terms of CO mass activity (**Supplementary Figure 6d, 7d**).

Next, we moved to cast our NiNC-IMI and NINC-PANI catalysts into cathode layers of single cell electrolyzers using spray-coating of aqueous inks. To achieve comparable morphological cathode layer qualities, Dynamic Light Scattering (DLS) helped optimize the average agglomerated particle size and ink suspension stability. First, the catalyst ink was diluted using isopropanol for a constant initial transmittance (~20%; NiNC-IMI 600 times; NiNC-PANI: 60 times), and each test lasted 40 mins. The diluted NiNC-IMI catalyst ink suspension showed high stability in our test. Its hydrodynamic radius stayed around 260 nm with constant transmittance. On the contrary, the radius of NiNC-PANI dropped from 900 nm to 500 nm during this period, and the suspension turned transparent due to faster particle precipitation (**Supplementary Figure 10**). These insights prompted adjustments in our ink deposition protocols to ensure comparable layer qualities.

A TEM/SEM microscopic analysis of the catalyst layer morphologies of NiNC-IMI and NiNC-PANI revealed important differences (**Figure 2h,i**). Larger-scale morphological differences of the two sprayed Gas Diffusion Electrode (GDE) layers became more obvious at higher-resolution SEM scales (**Figure 2j,k**) and cross-section SEM images (**Figure 2l,m**). Sponge-like channel structures with fine, dense, and homogeneously distributed pores and channels (around 3 um diameter) were revealed in the NiNC-IMI layer. By contrast, the NiNC-PANI catalyst layer showed larger but fewer channels (additional high resolution SEM images are shown in **Supplementary Figure 11**). Moreover, other physical characterizations, such as catalyst layer thickness, hydrophobicity, through-plane (TP) and in-plane (IP) conductivity, and gas permeability, were conducted on the sprayed GDEs, and the corresponding data are listed in **Supplementary Table 5**.

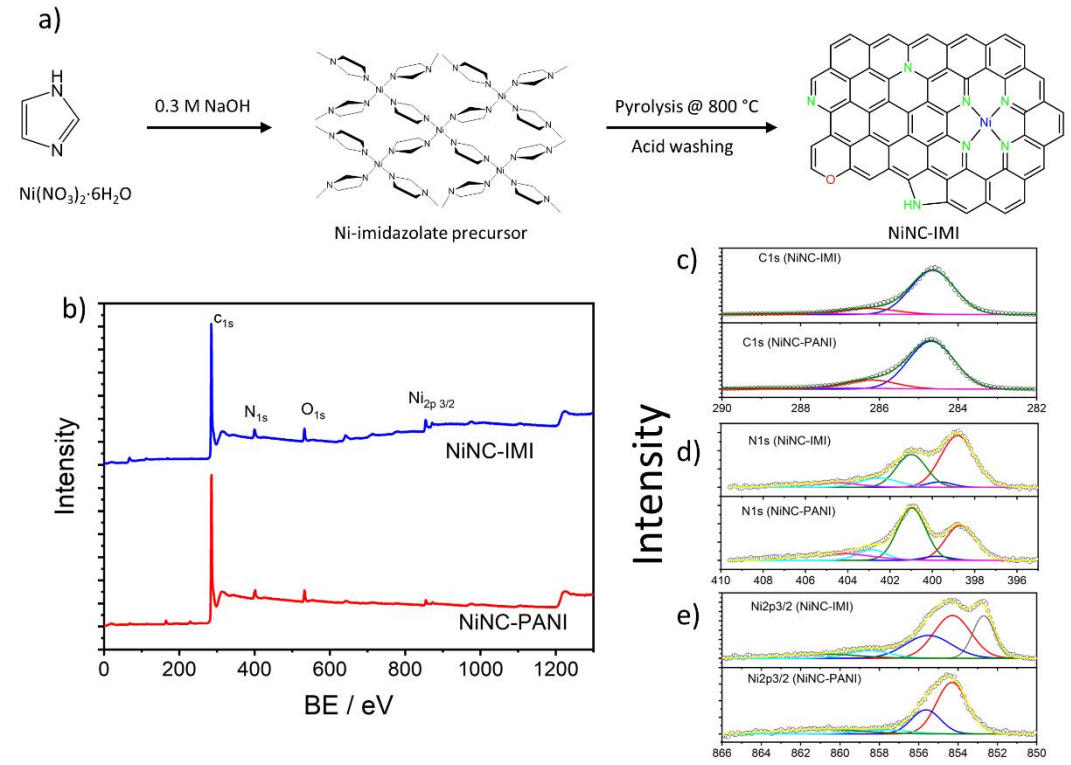
a)
0.3 M NaOH
Ni(NO3)2·6H2O
Ni-imidazolate precursor
Pyrolysis @ 800 °C
Acid washing
NiNC-IMI
b)
Intensity
C1s
N1s
O1s
Ni2p 3/2
NiNC-IMI
NiNC-PANI
BE / eV
c)
C1s (NiNC-IMI)
C1s (NiNC-PANI)
d)
N1s (NiNC-IMI)
N1s (NiNC-PANI)
e)
Ni2p3/2 (NiNC-IMI)
Ni2p3/2 (NiNC-PANI)
Intensity

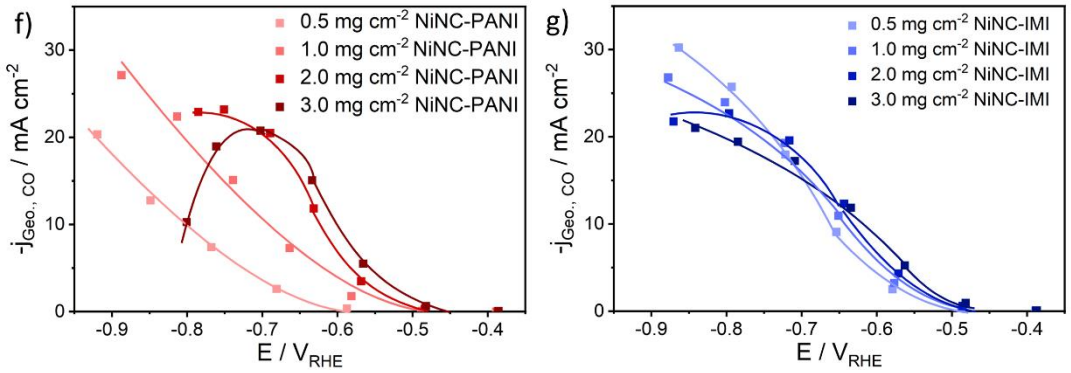
f)
0.5 mg cm-2 NiNC-PANI
1.0 mg cm-2 NiNC-PANI
2.0 mg cm-2 NiNC-PANI
3.0 mg cm-2 NiNC-PANI
-jGeo., CO / mA cm-2
E / VRHE
g)
0.5 mg cm-2 NiNC-IMI
1.0 mg cm-2 NiNC-IMI
2.0 mg cm-2 NiNC-IMI
3.0 mg cm-2 NiNC-IMI
-jGeo., CO / mA cm-2
E / VRHE

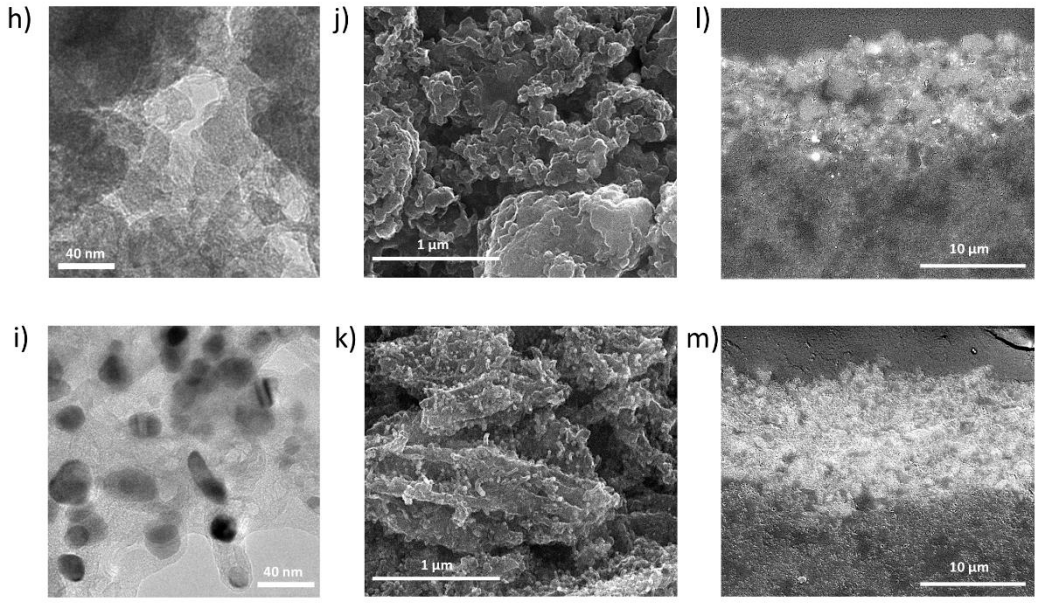
h)
40 nm
j)
1 µm
l)
10 µm
i)
40 nm
k)
1 µm
m)
10 µm

Figure 2: **Synthesis, characterisation and H-Cell performance screening.** a) Synthesis pathway of the NiNC-IMI catalyst via a Ni-imidazolate intermediate. b-e) Chemical state and surface composition of the as-prepared catalysts using X-ray photoessmison spectra. b) XPS survey of both catalysts, c) C1s spectra, d) N1s spectra and e) Ni2p 3/2spectra spectra profiles. Microscoupic images of our synthesized catalysts. Partial CO current density as function of the IR corrected cathode potential against Reversible hydrogen electrode of f) NiNC-PANI and g) NiNC-IMI. Catalyst loading is varied from 0.5 mg cm^{-2} to 3 mg cm^{-2} and all tests are performed in 0.5 M CO_2 saturate $KHCO_3$ solution. TEM images of the h) NiNC-PANI respectively i) NiNC-IMI catalyst powder. High resolution SEM images of the GDE catalyst layer of j) NiNC-PANI respectively k) NiNC-IMI. Field Emission Gun – Scanning Electron Microscope images (FEG-SEM) cross-section images of the l) NiNC-PANI and m) NiNC-IMI GDE.

Electrochemical CO_2-to-CO reduction performance in a zero-gap membrane electrode assembly single cell electrolyzers

Spray-coated GDEs were tested in a single-pass zero-gap membrane electrode assembly (MEA) flow electrolyzer cell incorporated in a customized test set up. The configuration of our electrolyzer (**Figure 3a**), testing platform (**Figure 3b**), mounting process (**Supplementary Figure 12a**) and a schematic zoom in of the cell (**Supplementary Figure 12b-e**) are illustrated. Volumetric electrolyzer outlet flow rates were tracked using a N_2 bleed (**Supplementary Figure 13**, **Supplementary Equation 8**) and used for subsequent reaction rate and carbon crossover diagnosis. NiNC-IMI and NiNC-PANI catalysts were tested at various geometric catalyst loadings. Prior to CO_2 electrolysis, the electrochemical cell impedance (**Supplementary Figure 14a and b)** revealed values of 0.21 (± 0.01) Ohm, independent of the catalyst loading. The catalytic CO_2-to-CO cell performance was screened from -50 mA cm^{-2} to -500 mA cm^{-2} (at 50 and 100 mA cm^{-2} increments). At he beginning of each break-in, a characteristic cathode potential overshoot up to -5.5 V appeared (**Supplementary Figure 14c and d**). This potential overshoot increased with catalyst loading, which is why we associate this with the ionic reinforcing and wetting process of the MEA and the bipolar junction between ionomer and membrane.

Key kinetic performance indicators (faradic CO efficiency, FE_{CO}, and partial CO current density, $J_{geo,\,CO}$) of the NiNC-based CO_2-to-CO electrolyzers are shown in **Figure 3c-f** (NiNC-IMI in blue, NiNC-PANI in red colors). For NiNC-IMI, FE_{CO} correlated inversely with the geometric catalyst loading. Other important electrolyzer cell performance parameters, rigorously

defined in **Supplementary Table 1**, yet often unreported previously, were evaluated and compared in the radar plots of **Figure 3g,h,i**.

At optimized 1.0 mg cm^{-2} catalyst loading, the FE_{CO} reached essentially 100% FE_{CO} up to a current densitiy of -200 mA cm^{-2}. FE_{CO} values of 90% and 85% FE_{CO} were measured at -250 mA cm^{-2} and -300 mA cm^{-2}, respectively, at a cell voltage of just above 3 V. What sets the present CO_2-to-CO electrolyzer cell performance sharply apart from previous reports is the uniquely low operating value of the stoichiometric excess of CO_2, λ_{stoich}, of about 1.2. λ_{stoich} is defined as the ratio of the volumetric CO_2 inflow and consumption rate, $\lambda_{\text{stoich}} = \frac{\dot{V}_{CO_2,in}}{\dot{V}_{CO_2,consumed}}$. This is why λ_{stoich} controls the molar CO_2:CO ratio, r_{CO2}, in the electrolyzer outlet. Given the experimental FE_{CO} ~ 100 % and taking CO_3^{2-} as the prevalent anion crossing the membrane (see cell diagnosis further below), r_{CO2} of the present NINC-IMI electrolyzer can be recast into $r_{CO_2} = \frac{\dot{V}_{CO_2,\ out}}{\dot{V}_{CO}} = 2(\lambda - 1)$ (**Supplementary Table 1)** and is around 0.4, implying that the outlet contains a record 70 mol% CO (balance CO_2), a previously unachieved CO-rich outlet stream. Also noteworthy is the overall energy efficiency of our NiNC-IMI cell of 40% at nearly 200 mA cm^{-2} cell current.

By contrast, using the NiNC-PANI reference catalysts, FE_{CO} > 90% was only achieved at low currents of -50 mA cm^{-2}, with loading having minor impact (**Figure 3c-d**). The polarization curve and j_{CO} are shown in the SI (**Supplementary Figure 15-16**). We measured double layer currents at different scan rates (**Supplementary Figure 17a-b**) and we found that the interfacial capacitance does correlate with the NiNC-IMI loading, yet does not for NiNC-PANI (**Supplementary Figure 17c**), further evidence for limited microporous site accessibility.

To better appreciate the unique overall performance of our CO_2-to-CO cell design, we contrast the set of kinetic NiNC-IMI GDE parameters to i) those of the reference NiNC-PANI GDE (**Figure 3g**), ii) to the best previously published NiNC GDEs (**Figure 3h**) and iii) to state-of-art Ag-based catalyst GDEs (**Figure 3i**) (details in **Supplementary Table 6**). The comparison attests to the present electrolyzer cell design as a uniquely favorable combination of performance indicators.

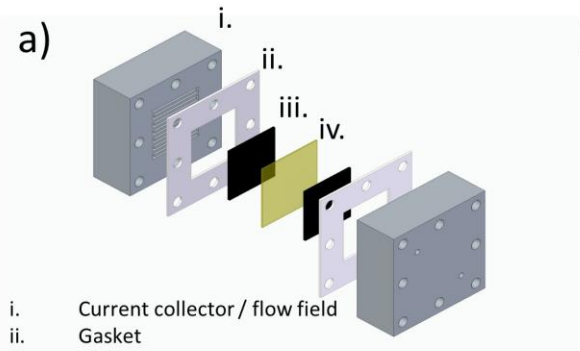

i. Current collector / flow field
ii. Gasket
iii. GDE
iv. Membrane

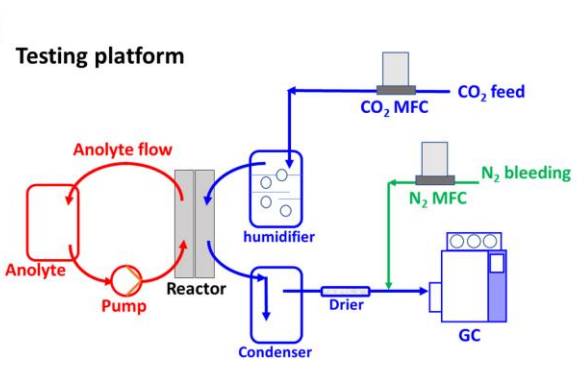

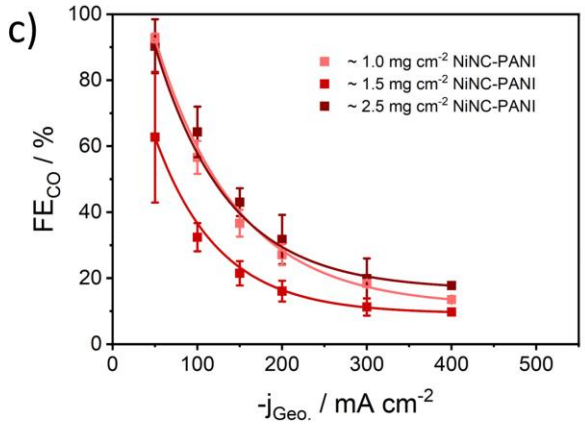

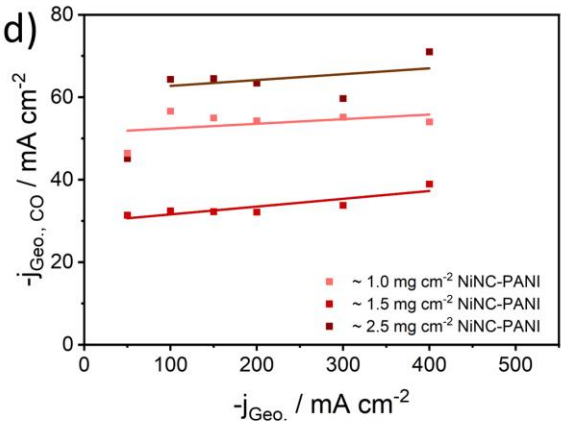

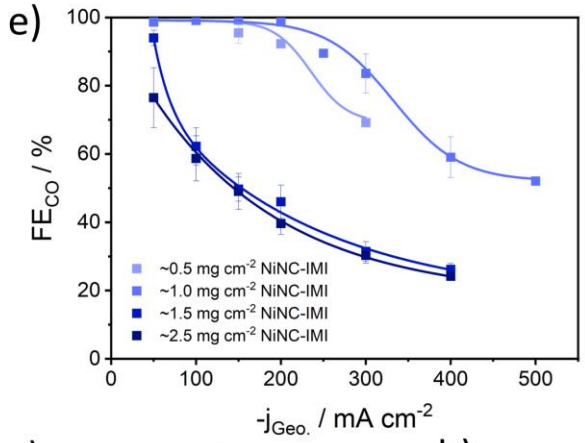

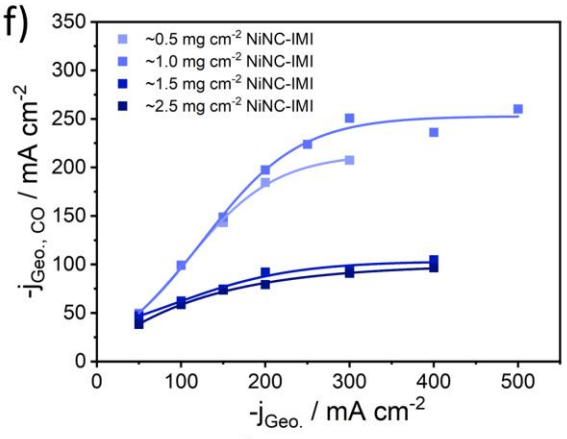

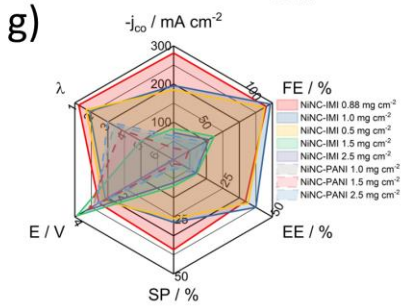

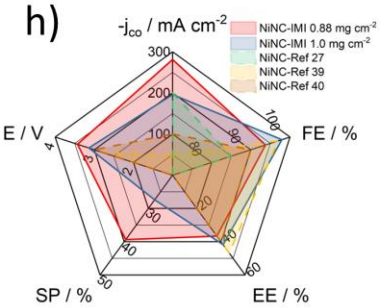

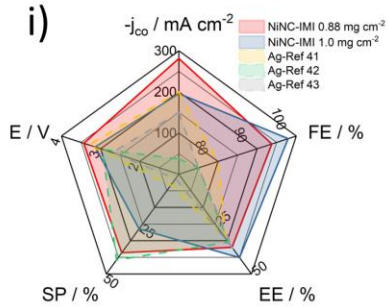

Figure 3: **CO_2 Electrolyzer performance tests in neutral-pH, zero gap cell configurations.** a) Scheme of our zero gap MEA cell for CO_2 reduction. b) Scheme of our testing platform. The electrolyte-freecathodic chamber was feed with humidified CO_2 (25 ml min^{-1}) and was separated to the anodic chamber using an AEM. 0.1 M $KHCO_3$ was recirculated as the anolyte, with a flow rate of 20 mL min^{-1}. The product stream was flowed through a condenser and dried usingmolecular sieve. A N_2 (2.5 ml min^{-1}) bleeding line is inserted as the flow rate internal standard.. c) The faradaic efficiency and d) CO partial current density as function of the total geometrical current of the NiNC-PANI catalyst with different loading. e) Faradaic efficiency and f) CO partial current density as function of the total geometrical current of a NiNC-IMI catalyst with different loading. The electrochemical performance was measured by holding each current density (0 to -500 mA cm^{-2}) for 15 mins with an GC injection after 14 min. Each data point represents the standard mean and error upon 3-5 measurements. Spider plots with relevant performance metrics as ($-j_{co}$, FE, EE, SP, E, λ) for the electrochemical reduction of CO_2 to CO of our NiNC-IMI catalyst in comparison to g) the NiNC-PANI reference, h) to date reported NiNC catalysts[28,39,40] and i) silver catalysts[41-43]

CO_2 consumption analysis and the Diagnostic Carbon Crossover Coefficient CCC

In this section, we propose the concept of a Carbon-Crossover-Coefficient (CCC) as a new experimental diagnostic tool for CO_2 electrolyzers. The CCC and its relation to FE_{CO} values reveal the nature of the dominant anion transport across the membrane, and point to origins of carbon mass transfer limitations within and across the cathode. Thereby, the CCC diagnosis helps improve GDE designs.

First, we recall that although the NiNC-IMI and NiNC-PANI catalysts delivered comparable apparent catalytic activities in the liquid-electrolyte H-cell setup, their MEA current density-FE_{CO} efficiency relations at varying catalyst loadings differed sharply. We attribute this to distinctly different final catalyst layer morphologies (**Figure 2i and m**). As a result of this, distinct CO_2 transfer kinetics in-plane and across the catalyst layers ensued. Paired with the non-catalytic, acid-base CO_2 consumption by catalytically generated OH- into HCO_3^- and CO_3^{2-} species inside the cathode (**Figure 4a)**, complex carbon mass transfer and consumption patterns arise (**Figure 4b,c)**.

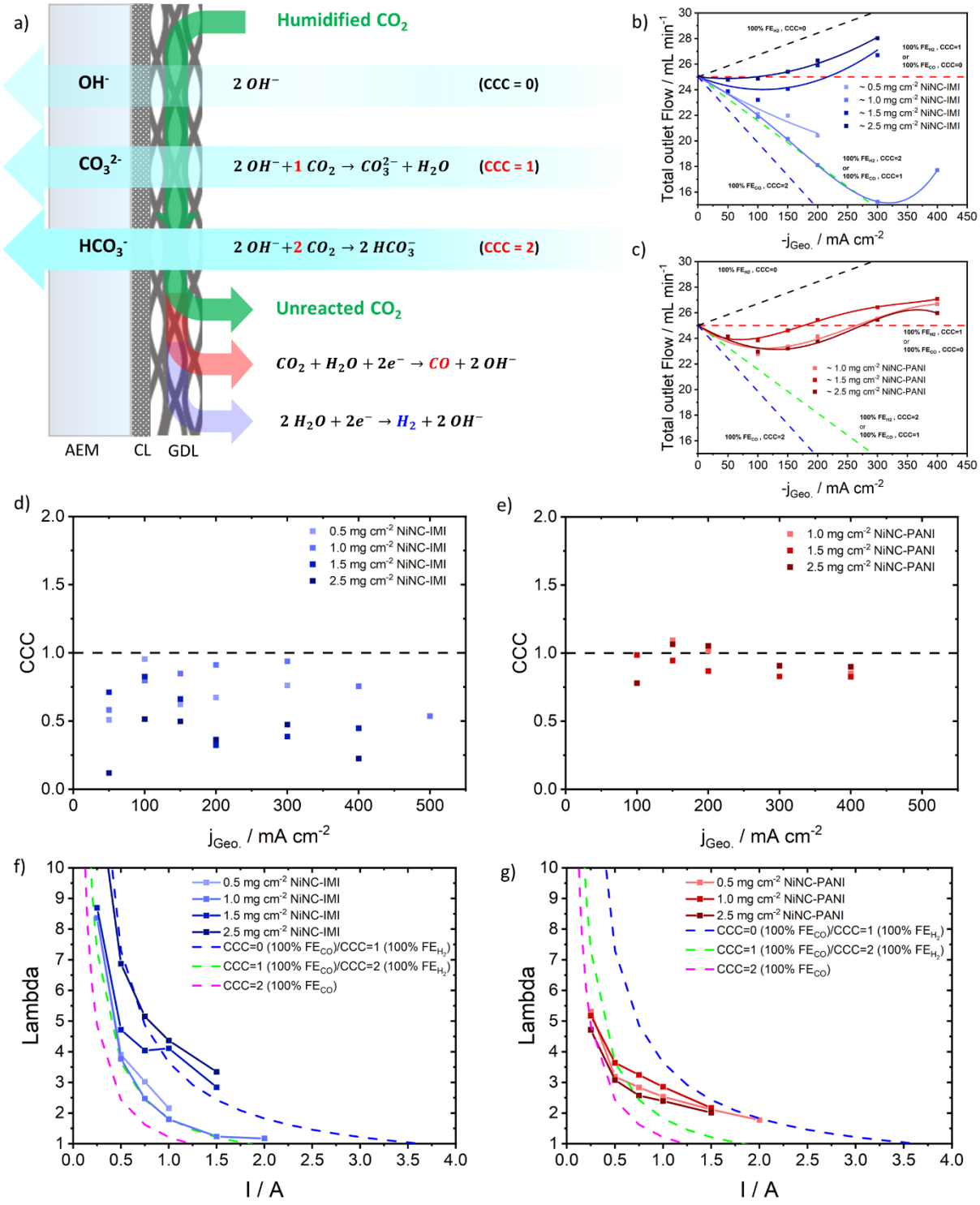

Figure 4: **CO_2 consumption, Carbon Crossover Coefficient, CCC, and Stoichiometric excess.** a) Schematic drawing of GDE structure and proposed reaction and mass transfer pathways in relation to the Carbon-Crossover-Coefficient, CCC. Derivation of CCC see **Supplementary Equations 9-19.** The theoretical exit flow rate vs applied current relations at varying CCC are shown in **Supplementary Figure 18**. B,c) Experimentally observed exit flow rates vs the applied geometric current for the b) NiNC-IMI and c) NiNC-PANI catalyst with model predictions (dashed lines) (see **Supplementary Note 4)** for all different anions (black dash line – 100% FE H_2,

CCC=0; red dash line – 100% FE H_2, CCC=1 or 100% FE CO, CCC=0; green dash line – 100% FE H_2, CCC=2 or 100% FE CO, CCC=1; blue dash line 100%FE CO, CCC=2) . CCC value as function of the applied geometric current density for d) NiNC-IMI and e) NiNC-PANI at different loadings. The stoichiometric CO2 exess, λ_{stoich} , (see also **Supplementary Table 1)** vs. the applied current for f) NiNC-IMI and g) NiNC-PANI catalyst with model predictions for different CCC and selectivities.

To better understand the carbon consumption mechanisms, we conceptually separate the carbon mass transfer inside the cathode into two. First, there is the in-plane carbon mass transfer to the active sites along the active MEA area, which triggers the catalytic CO_2 conversion and the non-catalytic acid-base CO_2 consumption. Second, there is the through-plane carbon transfer (via CO_3^{2-} or HCO_3^-, **Figure 4a)**. The through-plane carbon transfer leads to a current- and efficiency-dependent gas volume (flow rate) depletion in the cell outlet.[41,44,45] Based on this, we can formulate three limiting reaction-transport scenarios associated with mathematical correlations between the applied cell current, I_{cell}, the FE_{CO} and FE_{H2} values, and the electrolyzer exit flow rate ($\dot{V}_{Out}$) (**Supplementary Figure 18):**

1) For pure OH^- layer and membrane crossover, neither acid-base nor through-plane CO_2 depletion occurs. Electrochemical CO_2-to-CO conversion maintains the volume- and carbon- balance in the cathodic chamber, while the HER causes a current-controlled flow rate surplus (**Supplementary Figure 18a**).
2) In case of pure CO_3^{2-} crossover, every catalytically generated CO or H_2 molecule consumes one molecule of CO_2 for through-plane transfer. Now, the catalytic CO_2-to-CO conversion causes a current-dependent CO_2 and exit flow rate depletion due to the co-generated alkaliniy, with the HER helping to balance the gas volume (**Supplementary Figure 18b**).
3) In case of pure HCO_3^- transfer, every catalytically generated CO or H_2 molecule consumes two molecules of CO_2 for through-plane transfer, causing the highest CO_2 and exit gas volume depletion (**Supplementary Figure 18c**).

We now compare the three predicted limiting exit flow rate – current relations to the experimental data (**Figure 4b-c**). The dashed lines denote the limiting cases for perfect faradaic efficiencies according to **Supplementary Figure 18**. The solid lines are the experimental values. At low loadings (1.0 mg cm^{-2}, ~95% FE_{CO}) NiNC-IMI displayed an almost ideal flow depletion pattern over a wide current range, perfectly matching the predicted CO_3^{2-} through-plane transfer at FE_{CO}=100% , **Figure 4b**. By contrast, cells with higher catalyst loadings showed gradual volume surplus, attributed to a rising FE_{H2} and OH^- crossover. Conversely,

impact of the NINC-PANI loading was minor, never followed a limiting mass transfer case, and showed an increasing crossover of OH^- over CO_3^{2-}, **Figure 4c.**

To deconvolute the nature of the CO_2 consumption further, we now explicitely take the catalytic production rates of CO ($\dot{V}_{CO}$) and H_2 ($\dot{V}_{H_2}$) as well as the CO_2 input feed ($\dot{V}_{CO_2,in}$) and the exit flow rate ($\dot{V}_{out}$) into account. Starting from the gas volume and carbon balance (**Supplemental Note 5, Supplementary Equations 9-19**), we derive and define the experimentally accessible Carbon-Crossover-Coefficient (CCC) for the acid-base CO_2 depletion as

$$\mathrm{CCC} = \frac{\dot{V}_{H_2}+\dot{V}_{CO_2,in}-\dot{V}_{out}}{\dot{V}_{CO}+\dot{V}_{H_2}}. \qquad \text{Equation 1}$$

The CCC value can be perceived as the ratio between the non-catalytic acid-base CO_2 consumption rate and the rate of catalytic alkalinity production. It is experimentally easily accessible and reveals the nature of the prevalent anion crossing the membrane in an uniquely intuitive way: For CCC=0 there is pure OH^- transfer, for CCC=1 pure CO_3^{2-}crossover, and for CCC=2 pure HCO_3^{2-} crossover. A number of the kinetic electrolyzer performance parameters in **Supplementary Table 1** can be expressed in terms of the CCC.

The CCC value of NiNC-IMI electrolyzer cells at low loadings remained close to 1 (**Figure 4d**) suggesting prevalent CO_3^{2-} crossover. At higher NiNC-IMI catalyst loadings, the drop of the CCC value implies a gradual switch to OH^- transfer, which we attribute to CO_2 transfer limitations to the active sites. Indeed, as revealed by GEIS analysis, increased charge resistance (in low frequency region) emerges with high NiNC-IMI loadings (**Supplementary Figure 19**). By constrast, the NiNC-PANI loading showed minor impact on the CCC. The prevalent anion transport mechanism remained CO_3^{2-} crossover at all currents (**Figure 4e**).

Next, we relate the stoichiometric CO_2 ratio, $\lambda_{\mathrm{stoich}}$ (**Supplementary Table 1**), to the faradaic efficiency and applied currents (**Figures 4f,g)** and express it in terms of the CCC to obtain

$$\lambda_{\mathrm{stoich}} = \frac{\dot{V}_{CO_2,in}}{CCC\ (\dot{V}_{CO}+\dot{V}_{H_2})+\dot{V}_{CO}}\ . \qquad \text{Equation 3}$$

For 1 mg cm^{-2} NiNC-IMI, the experimentally determined values of $\lambda_{\mathrm{stoich}}$ followed the theoretical CCC = 1 line (green dashed) up to ca 1.5 A, associated with pure CO_3^{2-} transfer. With pure CO_3^{2-} transfer, the maximum CO_2 single pass conversion, SP, is limited to 50%, as

2 molecules CO_2 are consumed for each produced CO. Under these conditions, the NiNC-IMI cell (1 mg cm^{-2}) *SP* reaches the very high single pass conversion of 40% at -300 mA cm^{-2}, at a previously unachieved low λ_{stoich} = 1.2 (**Figure 4f**). As a result, our NiNC-IMI electrolyzer design delivers a CO concentrated exit stream.

Using the λ_{stoich} vs I plots, we can deepen our kinetic analysis further: The experimental values of λ_{stoich} of the NiNC-PANI cells remain larger due to their low FE_{CO} < 100%, i.e. because CO_2 is largely consumed for (bi)carbonate (**Figure 4g**). At higher loadings, the NiNC-IMI cells displayed larger λ_{stoich}, as well, however, this was due to their lower CCC=0 at FE_{CO} = 100% (**Figure 4f** blue dashed line), implying OH- as the prevalent anion.

To demonstrate the practical diagnostic value of the CCC and λ_{stoich} -based electrolyzer cell performance analysis, we consider the cell data in FE_{CO} vs. CCC plots (**Figure 5a)**. We *qualitatively* distinguish distinct regions (green, yellow, red) that we associate with distinct in-plane and through-plane transport as well as distinct catalytic CO_2 conversion. Operating electrolyzer conditions with CCC ~ 1 and low FE_{CO} < 60% (yellow in **Figure 5a**, **Figure 5c)** suggest poor in-plane CO_2 transfer to active sites and poor subsequent catalytic conversion, as seen for the NiNC-PANI electrolyzers: suboptimal microporous morphology caused poor site accessibility and flooded micropores result in low FE_{CO}, as confirmed by the microscopic analysis of the sprayed layer structure, and the loading-independent double-layer capacitance (**Supplementary Figure 17**). The loading-indepent value of CCC ~ 1 is testament to sufficiently effective ionic through-plane channels in the catalyst layer. This regime calls for adjustment of the catalyst pore size at constant layer thickness. Operating electrolyzer conditions with CCC ~ 1 and high FE_{CO}, as seen for NiNC-IMI cells at 1 mg cm^{-2} (green in **Figure 5a, Figure 5d**), attest to good site accessibility, layer thickness, and good in-plane and through-plane transport. By contrast, operating electrolyzer conditions with CCC << 1 and low FE_{CO}, as seen for NiNC-IMI cells at high loadings (red in **Figure 5a, Figure 5b**), are characterized by poor in-plane and poor through-plane transport. Insufficient through-plane ion channels exist, which is why ion transport is shifted toward OH^-. This regime suggests excessively thick catalyst layers.

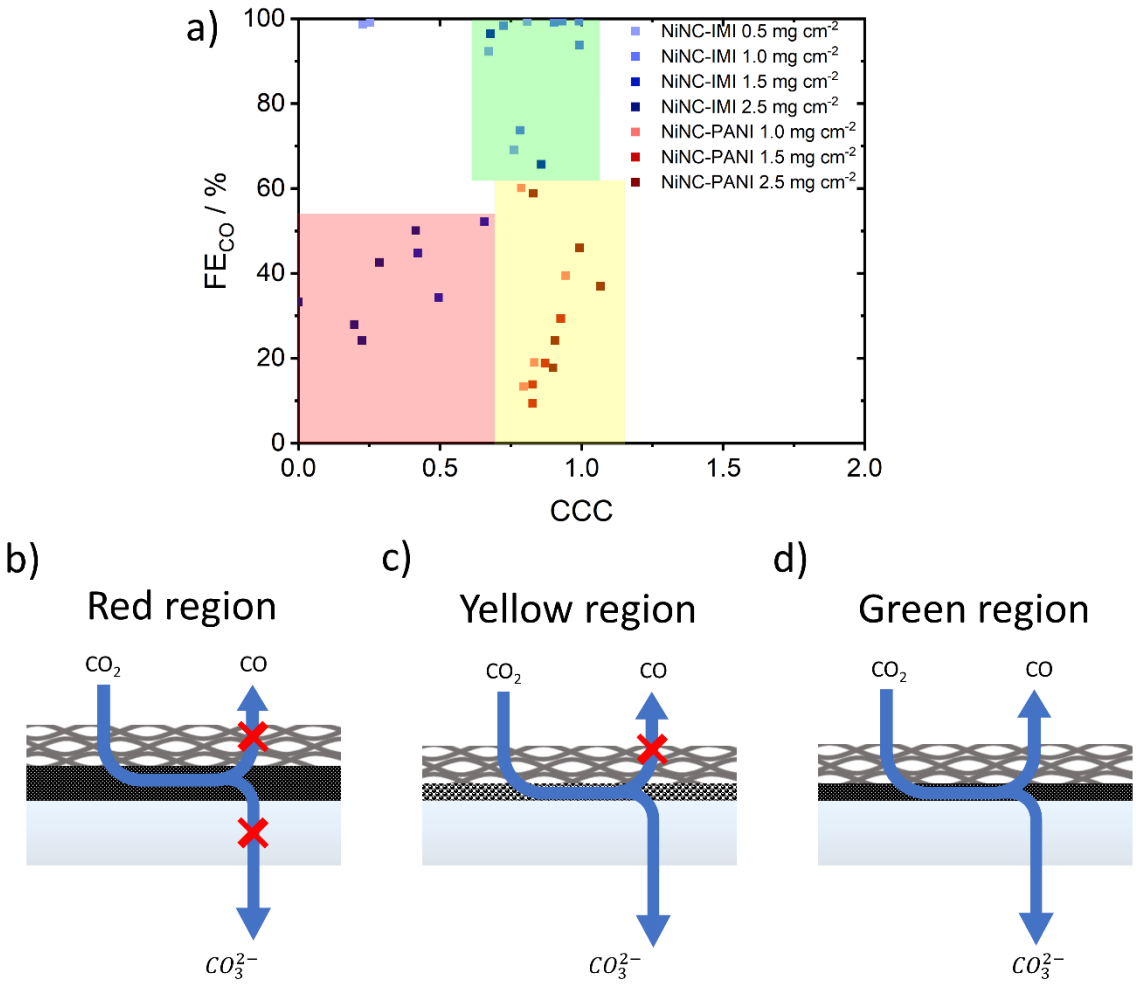

Figure 5: **Cell Diagnosis using Carbon-Crossover-Coefficient and Faradaic CO Efficiency.** a) Faradaic CO efficiency vs Carbon-Crossover-Coefficient plots yield distinct operating reaction-transport regimes (Red, Yellow, and Green) to diagnose the mass transfer limitations. Graphic illustration of controlling transport limitations in these 3 regions includes, b) red: limited through-plane mass transport (higher loadings of NiNC-IMI, thicker layer), c) yellow: good through-plane but inhibited in-plane mass transfer (NiNC-PANI) and d) green: optimal mass transport region (lower loadings NiNIC-IMI, thinner layer) showing optimal faradaic efficiencies.

We note that experimental values of CCC > 1.25 reliably identified catastrophic GDE flooding phenomena, where OH- ions reacted with excess CO_2 to bicarbonate due to a sudden blockage of active sites. Here, the CCC value again proofs as a valuable diagnostic failure analysis indicator. On the other hand, for electrolyzers operating under acidic conditions using Nafion membranes (not shown in this contribution), a consistent value of CCC = 0 ensued, as no anionic carbon species forms and crosses the cation exchange membrane. A value of CCC = 2, which would suggest a pure HCO_3^{2-} transfer, is yet to be observed experimentally.

Conclusions

We have presented a highly CO-selective, layered imidazolate framework-derived NiNC electrocatalyst (NiNC-IMI) for the efficient electrochemical CO_2 reduction to CO in zero-gap single cell electrolyzers. This catalyst exhibited a favorable geometric and mass-based CO activity in liquid-electrolyte H-cells, thanks to its high catalytic active Ni-N_x site density and good site accessibility compared to a polyaniline-derived NiNC-PANI reference catalyst. We associate these favorable properties with its unique mesoporous structure over the microporous characteristics of the NiNC-PANI.

The NiNC-IMI catalysts were cast into cathode layers of varying catalyst loadings, which were deployed into zero-gap AEM electrolyzer cells. Operated under neutral-pH anolyte conditions, the NiNC-IMI CO_2-to-CO electrolyzer design outperformed state-of-art Ag and previously reported NiNC cathodes. Under optimized catalyst loading and layer thickness, the experimental faradaic CO efficiency, FE_{co}, reached 100% up to a current density of -200 mA cm^{-2} (E_{cell} ~ 3 V) and remained at 85% at -300 mA cm^{-2} (E_{cell} = 3.5 V). Beyond these popular performance metrics, we rigorously defined and experimentally considered a number of additional kinetic cell performance indicators, such as single pass conversion, SP, stoichiometric CO_2 excess, λ_{stoich}, and total energy efficiency, EE.

Unlike earlier reports, our present CO_2-to-CO electrolyzer design concomitantly displayed close to 80% CO_2 utilization efficiency, 40% single pass conversion to CO, 40% total energy efficiency, EE, and an uniquly low λ_{stoich}value of 1.2, which translated into molar CO ratio of 70% in the exit flow. Such CO-rich mixed feeds offer superior C2+ production rates when coupled to a second CO_2 conversion electrolyzer tandem cell[46].

Beyond the cell design, we proposed and validated new diagnostic tools for CO_2 electrolyzers to deconvolute catalytic and non-catalytic CO_2 consumption. We defined an experimentally accessible Carbon-Crossover-Coefficient (CCC) as the ratio between non catalytic CO_2 consumption and generated alkalinity. The CCC values of 0,1, and 2 were associated with the three physically limiting conditions of pure OH^-, CO_3^{2-}, and HCO_3^{2-} transport. We also showed how CCC-FE_{CO} maps define regions of distinct in-plane and through-plane transport regimes. Their diagnostic character reveals imperfections of CO_2 cathode layers and thereby helps improve electrolyzer designs. More broadly, the concept of the CCC diagnosis can be applied to other types of CO_2 electrolyzer cells, for instance, those converting CO_2 to hydrocarbons on

Cu-based catalysts, though the mathematical expressions will become more complex due to a broader product spectrum.

Methods

Synthesis protocol of the Imidaozlate derived Ni-N-C catalysts

Synthesis of NiNC-IMIdazolate precursor

The NiNC-IMIdazolate was synthesized following previous literature approach[47]. 8.724 g $Ni(NO_3)_2 \cdot 6H_2O$ (0.03 mol) and 24.0 g imidazole were mixed and stirred in 600 mL DI-Water. 1200 mL 0.3 M NaOH was dropped into the aforementioned mixture with a titration speed of 60 mL min^{-1}. After 6 hours stirring, the mixture was vacuum filtered and washed till neutral pH. The residual yellow powder was freeze dried and named as NiNC-IMIdazolate precursor.

Synthesis of Imidazolate-derived Ni-N-C

The NiNC-IMIdazolate precursor was placed in tube furnace and annealed at 800 °C for 3 h (ramping: 5.0 °C min^{-1}) under N_2 atmosphere (~ 80 ml min^{-1}). The carbonized powder was dispersed in 200 mL H_2SO_4 (ca. 1 M) at 80 °C and stirred for 10 hours. The acid washed sample was collected and washed with DI water until neutral pH and freeze dried to the as-prepared catalyst.

Synthesis of the reference Ni-N-C catalyst

The PANI-derived was identical with our previous published approach. 3 ml of aniline, 5 g $NiCl_2 \cdot 6H_2O$ and 5 g ammonium persulfate (APS, $(NH_4)_2S_2O_8$) was mixed in 0.5 L of 1 M HCl and stirred for 1 hour. The suspension was stirred for 48 hours after adding 0.4 g of dispersed activated Ketjen 600 carbon. The liquid suspension was thereafter dried at 95 °C for 24 hours, and residual solid mixture was ball-milled with Zr_2O_3 balls for 20 min.

The pyrolysis is carried in a furnace with a ramp of 30°C min^{-1} to 900 °C and kept at this temperature for 1 hour, in N_2 condition. Acid washing step in (2M H_2SO_4 at 90 °C for overnight) was performed to remove the excessive Ni particles. In this synthesis, 4 times heat treatment and 3 times acid washing was performed by turn, and the catalyst is obtained after the 4th

pyrolysis (Pyrolysis/Acid-washing/ Pyrolysis/Acid-washing/ Pyrolysis/Acid-washing/Pyrolysis).

Catalysts characterization: BET, SEM, TEM, and XPS

N2 sorption measurements was carried out using a Quantachrome Quadrasorb SI instrument with degassing temperature of 200 °C for 6 h for carbon samples and 120 °C for 12 h for NiNC-IMI samples before the measurement. The specific surface areas were calculated by using Brunauer-Emmett-Teller (BET) calculations and the pore size distributions were obtained from the adsorption branch of isotherms by the non-localized density functional theory (NLDFT) model. Scanning electron microscope (SEM) was measured using Gemini SEM 500 low vacuum high-resolution SEM.. Cross-section SEM images were obtained with SEM/FEG Inspect F 50 – FEI. Transmission electron microscope (TEM) was performed using FEI Tecnai G^2 20 S-TWIN electron microscope with an operating voltage of 200 kV. The conductivity was measured with Yokogawa GS610 Sourcemeter unit in galvanostatic mode between -2 mA and +2 mA in 0.2 mA steps. XPS (X-ray photoemission spectra) was conducted on a K-Alpha X-ray photoelectron spectrometer system (Thermo Scientific) with Hemispheric 180° dual-focus analyzer with 128-channel detector. X-ray monochromator was microfocused Al Kα radiation. The samples were pasted and pressed onto the sample holder using carbon taps for measurement.

Gas diffusion electrode preparation

85 mg as-prepared catalyst, 300 mg Nafion solution (Sigma-Aldrich, 5wt% Nafion in ethanol solution), 100 μL DI-water and 2900 μL isopropanol were mixed and sonificated using sonifer horn for 15 mins. The prepared ink was sprayed coated onto the commercial gas diffusion electrode provided by DeNora (GDL2), on the micro porous layer, at 80 °C.

MEA cell manufacture

A membrane electrode assembly type electrolyzer setup is deployed for the CO2RR performance testing, and the assembling procedure is illustrated in **Supplementary Figure 12**. The cathode GDL (5 cm^2), membrane (Sustainion membrane X37-50 RT, Dioxide material), and the anode material (5 cm^2, IrO2-GDE from Dioxide material) are layer by layer assembled in the electrolyzer. Both cathode and anode are located and stabilized in PTFE gaskets

(thickness: 200 microns; window size: 5 cm^2). After that, the cathode/membrane/anode layers are compressed within the electrolyzer plates (serving as flow fields and electron conductor) to ensure the reactor tightness, the electrode charge conductivity, and the ionic conductivity in the MEA.

MEA cell test station

The MEA cell CO2RR testing configuration is presented in **Figure 3a-b**. In the MEA cell testing protocol, no catholyte is applied. The humidified CO_2 gas flow is driven by a mass flow controller (MFC, Bronkhorst; flow rate: 25 mL min^{-1}) into the cathode flow field for the reaction. After the reaction, the product stream (out from the reactor) is purged through the condenser and drier, then mixed with a N_2 bleeding (2.5 mL min^{-1}) for GC analysis. In the anode chamber, $KHCO_3$ solution is recycled at a 20 mL min^{-1} flow rate.

All the CO2RR performance screening in this report is done at ambient temperature and pressure. The anode and cathode are connected with a potentiostat (Bio-Logic SP150 with a booster channel) to control the current densities. The reference electrode accompanies the anode for a two-electrodes configuration, and Potentio- and Galvano- electrochemical impedance spectra (PEIS and GEIS modules) are carried out to measure the cell-resistance. The CO2RR performance is assessed at various current densities. Each current step is held for 15 min before moving on to the next current setting, and the gas stream is injected in the GC sample loop at 14.5 min of each current step.

When driving the CO2RR in the flow cell, especially at large current densities, significant (bi-)carbonate crossover should be considered, which cause obvious flow rate depletion. Therefore, the N_2 bleeding line implemented in our scheme with a defined flow rate (2.5 mL min^{-1}) serves as an internal standard flow rate.

Product analysis

A Shimadzu 2014 on-line GC is utilized for product quantification. The gas stream is separated by the Hayesep Q + R columns and then analyzed by the TCD (Thermo Conductivity Detector) and FID (Flame Ionization Detector). The TCD detects the volume percentage ($\%_{VOL}$) of the H_2 product, and the FID measures the CO after being methanized. On the all Ni-N-C type catalyst, no liquid product is found after the electrolysis.

ACKNOWLEDGMENTS

Funding: The research leading to these results has received funding from the European Union's Horizon 2020 research and innovation programme under grant agreement No 85144, SELECTCO2.

Author contributions

S.B, W.J. and P.S. conceived and designed the project and wrote the manuscript. Q.F. and W.J. carried out the materials synthesis. S.B. and W.J characterization and electrochemical evaluation. M.K performed the TEM and XPS characterizations. D.G. and A.T. performed the SEM characterization. S.O. performed the BET characterization. All authors read and commented on the manuscript.

Declaration of interests

The authors declare no competing interest.

Additional information

Supplementary Information

The Supplementary Information is available free of charge on the XXXX website at DOI: XXXX.

Reference

1 *Global Energy Review 2020*, <www.iea.org/reports/global-energy-review-2020> (2020).

2 Jouny, M., Luc, W. & Jiao, F. General Techno-Economic Analysis of CO 2 Electrolysis Systems. *Industrial & Engineering Chemistry Research* **57**, 2165–2177, doi:10.1021/acs.iecr.7b03514 (2018).

3 Jourdin, L., Sousa, J., van Stralen, N. & Strik, D. P. B. T. B. Techno-economic assessment of microbial electrosynthesis from CO2 and/or organics: An interdisciplinary roadmap towards future research and application. *Applied Energy* **279**, 115775, doi:10.1016/j.apenergy.2020.115775 (2020).

4 Kibria, M. G. *et al.* Electrochemical CO 2 Reduction into Chemical Feedstocks: From Mechanistic Electrocatalysis Models to System Design. *Advanced Materials* **31**, 1807166, doi:10.1002/adma.201807166 (2019).

5 Lin, R., Guo, J., Li, X., Patel, P. & Seifitokaldani, A. Electrochemical Reactors for CO2 Conversion. *Catalysts* **10**, 473, doi:10.3390/catal10050473 (2020).

6 Verma, S., Kim, B., Jhong, H.-R. M., Ma, S. & Kenis, P. J. A. A Gross-Margin Model for Defining Technoeconomic Benchmarks in the Electroreduction of CO 2. *ChemSusChem* **9**, 1972–1979, doi:10.1002/cssc.201600394 (2016).

7 Luna, P. d. *et al.* What would it take for renewably powered electrosynthesis to displace petrochemical processes? *Science* **364**, doi:10.1126/science.aav3506 (2019).

8 Jhong, H.-R. M., Ma, S. & Kenis, P. J. A. Electrochemical conversion of CO2 to useful chemicals: current status, remaining challenges, and future opportunities. *Current Opinion in Chemical Engineering* **2**, 191–199, doi:10.1016/j.coche.2013.03.005 (2013).

9 Küngas, R. Review—Electrochemical CO 2 Reduction for CO Production: Comparison of Low- and High-Temperature Electrolysis Technologies. *Journal of The Electrochemical Society* **167**, 044508, doi:10.1149/1945-7111/ab7099 (2020).

10 Lee, M.-Y. *et al.* Current achievements and the future direction of electrochemical CO 2 reduction: A short review. *Critical Reviews in Environmental Science and Technology* **50**, 769–815, doi:10.1080/10643389.2019.1631991 (2020).

11 Alerte, T. *et al.* Downstream of the CO 2 Electrolyzer: Assessing the Energy Intensity of Product Separation. *ACS Energy Letters* **6**, 4405–4412, doi:10.1021/acsenergylett.1c02263 (2021).

12 Siahrostami, S., Bjorketun, M. E., Strasser, P., Greeley, J. & Rossmeisl, J. Tandem cathode for proton exchange membrane fuel cells. *Phys Chem Chem Phys* **15**, 9326-9334, doi:Doi 10.1039/C3cp51479j (2013).

13 Jouny, M., Hutchings, G. S. & Jiao, F. Carbon monoxide electroreduction as an emerging platform for carbon utilization. *Nature Catalysis* **2**, 1062–1070, doi:10.1038/s41929-019-0388-2 (2019).

14 Hori, Y., Wakebe, H., Tsukamoto, T. & Koga, O. Electrocatalytic process of CO selectivity in electrochemical reduction of CO2 at metal electrodes in aqueous media. *Electrochimica Acta* **39**, 1833-1839, doi:10.1016/0013-4686(94)85172-7 (1994).

15 Tornow, C. E., Thorson, M. R., Ma, S., Gewirth, A. A. & Kenis, P. J. A. Nitrogen-Based Catalysts for the Electrochemical Reduction of CO 2 to CO. *Journal of the American Chemical Society* **134**, 19520–19523, doi:10.1021/ja308217w (2012).

16 Nam, D.-H. *et al.* Intermediate Binding Control Using Metal–Organic Frameworks Enhances Electrochemical CO 2 Reduction. *Journal of the American Chemical Society* **142**, 21513–21521, doi:10.1021/jacs.0c10774 (2020).

17 Kim, B., Hillman, F., Ariyoshi, M., Fujikawa, S. & Kenis, P. J. A. Effects of composition of the micro porous layer and the substrate on performance in the electrochemical reduction of CO2 to CO. *Journal of Power Sources* **312**, 192–198, doi:10.1016/j.jpowsour.2016.02.043 (2016).

18 Lee, W. H. *et al.* Highly selective and scalable CO2 to CO - Electrolysis using coral-nanostructured Ag catalysts in zero-gap configuration. *Nano Energy* **76**, 105030, doi:10.1016/j.nanoen.2020.105030 (2020).

19 Dinh, C.-T., García de Arquer, F. P., Sinton, D. & Sargent, E. H. High Rate, Selective, and Stable Electroreduction of CO 2 to CO in Basic and Neutral Media. *ACS Energy Letters* **3**, 2835–2840, doi:10.1021/acsenergylett.8b01734 (2018).

20 Nwabara, U. O., Cofell, E. R., Verma, S., Negro, E. & Kenis, P. J. A. Durable Cathodes and Electrolyzers for the Efficient Aqueous Electrochemical Reduction of CO 2. *ChemSusChem* **13**, 855–875, doi:10.1002/cssc.201902933 (2020).

21 Weekes, D. M., Salvatore, D. A., Reyes, A., Huang, A. & Berlinguette, C. P. Electrolytic CO 2 Reduction in a Flow Cell. *Accounts of Chemical Research* **51**, 910–918, doi:10.1021/acs.accounts.8b00010 (2018).

22 Cofell, E. R., Nwabara, U. O., Bhargava, S. S., Henckel, D. E. & Kenis, P. J. A. Investigation of Electrolyte-Dependent Carbonate Formation on Gas Diffusion Electrodes for CO 2 Electrolysis. *ACS Applied Materials & Interfaces* **13**, 15132–15142, doi:10.1021/acsami.0c21997 (2021).

23 Kaczur, J. J., Yang, H., Liu, Z., Sajjad, S. D. & Masel, R. I. Carbon Dioxide and Water Electrolysis Using New Alkaline Stable Anion Membranes. *Frontiers in Chemistry* **6**, doi:10.3389/fchem.2018.00263 (2018).

24 Varela, A. S. *et al.* Metal-Doped Nitrogenated Carbon as an Efficient Catalyst for Direct CO2 Electroreduction to CO and Hydrocarbons. *Angew Chem Int Ed Engl* **54**, 10758-10762, doi:10.1002/anie.201502099 (2015).

25 Torbensen, K. *et al.* Molecular Catalysts Boost the Rate of Electrolytic CO 2 Reduction. *ACS Energy Letters* **5**, 1512–1518, doi:10.1021/acsenergylett.0c00536 (2020).

26 Ren, S. *et al.* Molecular electrocatalysts can mediate fast, selective CO 2 reduction in a flow cell. *Science* **365**, 367–369, doi:10.1126/science.aax4608 (2019).

27 Nguyen, T. N., Salehi, M., van Le, Q., Seifitokaldani, A. & Dinh, C. T. Fundamentals of Electrochemical CO 2 Reduction on Single-Metal-Atom Catalysts. *ACS Catalysis* **10**, 10068–10095, doi:10.1021/acscatal.0c02643 (2020).

28 Möller, T. *et al.* Efficient CO 2 to CO electrolysis on solid Ni–N–C catalysts at industrial current densities. *Energy & Environmental Science* **12**, 640–647, doi:10.1039/c8ee02662a (2019).

29 Zhang, T. *et al.* Nickel–Nitrogen–Carbon Molecular Catalysts for High Rate CO 2 Electro-reduction to CO: On the Role of Carbon Substrate and Reaction Chemistry. *ACS Applied Energy Materials* **3**, 1617–1626, doi:10.1021/acsaem.9b02112 (2020).

30 Ju, W. *et al.* Understanding activity and selectivity of metal-nitrogen-doped carbon catalysts for electrochemical reduction of CO2. *Nature Communications* **8**, doi:10.1038/s41467-017-01035-z (2017).

31 Li, C. *et al.* Covalent Organic Framework (COF) derived Ni-N-C Catalysts for Electrochemical CO2 Reduction: Unraveling Fundamental Kinetic and Structural Parameters of the Active Sites. *Angewandte Chemie International Edition*, doi:10.1002/anie.202114707 (2022).

32 Koshy, D. M. *et al.* Understanding the Origin of Highly Selective CO2 Electroreduction to CO on Ni,N-doped Carbon Catalysts. *Angew Chem Int Ed Engl* **59**, 4043-4050, doi:10.1002/anie.201912857 (2020).

33 Zhang, H. *et al.* High-performance fuel cell cathodes exclusively containing atomically dispersed iron active sites. *Energy & Environmental Science* **12**, 2548-2558, doi:10.1039/c9ee00877b (2019).

34 Jakub, Z. *et al.* Nickel Doping Enhances the Reactivity of Fe 3 O 4 (001) to Water. *The Journal of Physical Chemistry C* **123**, 15038–15045, doi:10.1021/acs.jpcc.9b02993 (2019).

35 Liu, S. *et al.* Elucidating the Electrocatalytic CO 2 Reduction Reaction over a Model Single‐Atom Nickel Catalyst. *Angewandte Chemie International Edition* **59**, 798‐803, doi:10.1002/anie.201911995 (2020).

36 Yang, H. B. *et al.* Atomically dispersed Ni(i) as the active site for electrochemical CO2 reduction. *Nature Energy* **3**, 140–147, doi:10.1038/s41560-017-0078-8 (2018).

37 Soriano, L. *et al.* Surface effects in the Ni 2p x-ray photoemission spectra of NiO. *Physical Review B* **75**, doi:10.1103/PhysRevB.75.233417 (2007).

38 Vijay, S. *et al.* Unified mechanistic understanding of CO2 reduction to CO on transition metal and single atom catalysts. *Nature Catalysis* **4**, 1024–1031, doi:10.1038/s41929-021-00705-y (2021).

39 Jiang, K. *et al.* Isolated Ni single atoms in graphene nanosheets for high-performance CO2 reduction. *Energy & Environmental Science* **11**, 893-903, doi:10.1039/c7ee03245e (2018).

40 Daiyan, R. *et al.* Transforming active sites in nickel–nitrogen–carbon catalysts for efficient electrochemical CO2 reduction to CO. *Nano Energy* **78**, doi:10.1016/j.nanoen.2020.105213 (2020).

41 Larrazábal, G. O. *et al.* Analysis of Mass Flows and Membrane Cross-over in CO 2 Reduction at High Current Densities in an MEA-Type Electrolyzer. *ACS Applied Materials & Interfaces* **11**, 41281–41288, doi:10.1021/acsami.9b13081 (2019).

42 Jeng, E. & Jiao, F. Investigation of CO2 single-pass conversion in a flow electrolyzer. *Reaction Chemistry & Engineering* **5**, 1768-1775, doi:10.1039/d0re00261e (2020).

43 Lees, E. W. *et al.* Linking gas diffusion electrode composition to CO2 reduction in a flow cell. *Journal of Materials Chemistry A* **8**, 19493-19501, doi:10.1039/d0ta03570j (2020).

44 Larrazábal, G. O., Ma, M. & Seger, B. A Comprehensive Approach to Investigate CO 2 Reduction Electrocatalysts at High Current Densities. *Accounts of Materials Research* **2**, 220–229, doi:10.1021/accountsmr.1c00004 (2021).

45 Ma, M. *et al.* Insights into the carbon balance for CO 2 electroreduction on Cu using gas diffusion electrode reactor designs. *Energy & Environmental Science* **13**, 977–985, doi:10.1039/d0ee00047g (2020).

46 Wang, X. *et al.* Mechanistic reaction pathways of enhanced ethylene yields during electroreduction of CO(2)-CO co-feeds on Cu and Cu-tandem electrocatalysts. *Nat Nanotechnol* **14**, 1063-1070, doi:10.1038/s41565-019-0551-6 (2019).

47 Masciocchi, N., Castelli, F., Forster, P. M., Tafoya, M. M. & Cheetham, A. K. Synthesis and characterization of two polymorphic crystalline phases and an amorphous powder of nickel(II) bisimidazolate. *Inorg Chem* **42**, 6147-6152, doi:10.1021/ic034619o (2003).